Science
AAAS

Growth of Uniformly Oriented Silica MFI and BEA Zeolite Films on Substrates

Tung Cao Thanh Pham, *et al.*

Science **334**, 1533 (2011);
DOI: 10.1126/science.1212472

Science (print ISSN 0036-8075; online ISSN 1095-9203) is published weekly, except the last week in December, by the American Association for the Advancement of Science, 1200 New York Avenue NW, Washington, DC 20005.

photocurrent losses. The IQE of the two devices using large bandgap QDs (1.35 eV and 1.48 eV) exhibited peak quantum efficiencies consistent with the 85% plateau for photon energies below the MEG threshold; thus, we estimate the intrinsic photocurrent losses at ~15%. We attribute these losses to electron-hole recombination before carrier separation and collection as photocurrent and therefore normalize the measured IQE to these values, yielding the purple circles in Fig. 3C. These values compare well with a model (*7*) that accounts for a competition between MEG and hot-exciton cooling (Fig. 3C, solid black curve, dashed curve normalized as above). Finally, we applied a least-squares linear fit of a normalized version of the same model (*24*) to the IQE for the 0.72 eV solar cell in Fig. 3B, yielding $\eta_{MEG} = 0.62 \pm 0.1$, and an MEG onset threshold E_{th} (Eq. 2)

$$E_{th} = \left(1 + \frac{1}{\eta_{MEG}}\right) E_g = (2.61 \pm 0.03) E_g \quad (2)$$

indicating quantitative agreement with spectroscopic measurements. We believe this result constitutes incontrovertible evidence that MEG is more efficient in PbSe QDs than in bulk PbSe, which exhibits a MEG efficiency of only 0.31 and a corresponding onset of 4.22 E_g (*7*, *30*). To estimate the impact of MEG on the PCE, we integrated the 0.72 eV device IQE in excess of the baseline 85% (fig. S7, shaded region) against the AM1.5G solar spectrum. We estimate that ~1 mA cm^{-2}, or ~4%, of the total photocurrent arises from MEG, consistent with previous estimates based on TAS measurements of MEG in colloidal QDs (*7*). Bulk Si photovoltaic cells could only benefit by <1% from impact ionization, and $Si_{1-x}Ge_x$ alloys could benefit by at most 2% (*29*).

The useful effects of our hydrazine treatment allow multiple carriers produced by MEG to be efficiently collected in a solar cell made from electronically coupled QDs. To have the largest impact on solar energy conversion efficiency, the MEG onset would have to be close to twice the bandgap, which could lead to a bonus photocurrent contribution as high as 30% (*1*, *7*). The challenge is to learn how to further improve the MEG-enhanced quantum efficiency and this will necessarily involve maximizing the MEG kinetics by chemical, dimensional, or architectural means, while also limiting the inelastic, phonon-mediated exciton cooling rates. Carbon nanotubes (*31*, *32*) and PbSe nanorods (*33*) have shown promising results in this direction. Our findings are a first step toward breaking the single junction Shockley-Queisser limit (*34*) of present-day first and second generation solar cells, thus moving photovoltaic cells toward the third-generation regime.

References and Notes

1. M. C. Hanna, A. J. Nozik, *J. Appl. Phys.* **100**, 074510 (2006).
2. A. J. Nozik, *Physica E* **14**, 115 (2002).
3. L. R. Canfield, R. E. Vest, R. Korde, H. Schmidtke, R. Desor, *Metrologia* **35**, 329 (1998).
4. The MEG efficiency, η_{MEG}, is related to the number of additional excitons generated per additional bandgap of energy carried by an absorbed photon after the threshold photon energy for MEG is passed.
5. J. A. McGuire, M. Sykora, J. Joo, J. M. Pietryga, V. I. Klimov, *Nano Lett.* **10**, 2049 (2010).
6. C. Delerue, G. Allan, J. J. H. Pijpers, M. Bonn, *Phys. Rev. B* **81**, 125306 (2010).
7. M. C. Beard *et al.*, *Nano Lett.* **10**, 3019 (2010).
8. G. Nair, L. Y. Chang, S. M. Geyer, M. G. Bawendi, *Nano Lett.* **11**, 2145 (2011).
9. J. A. McGuire, J. Joo, J. M. Pietryga, R. D. Schaller, V. I. Klimov, *Acc. Chem. Res.* **41**, 1810 (2008).
10. A. G. Midgett, H. W. Hillhouse, B. K. Huges, A. J. Nozik, M. C. Beard, *J. Phys. Chem. C* **114**, 17486 (2010).
11. M. C. Beard, *J. Phys. Chem. Lett.* **2**, 1282 (2011).
12. J. B. Sambur, T. Novet, B. A. Parkinson, *Science* **330**, 63 (2010).
13. V. Sukhovatkin, S. Hinds, L. Brzozowski, E. H. Sargent, *Science* **324**, 1542 (2009).
14. D. V. Talapin, J. S. Lee, M. V. Kovalenko, E. V. Shevchenko, *Chem. Rev.* **110**, 389 (2010).
15. J. M. Luther *et al.*, *ACS Nano* **2**, 271 (2008).
16. J. M. Luther *et al.*, *Nano Lett.* **7**, 1779 (2007).
17. M. C. Beard *et al.*, *Nano Lett.* **9**, 836 (2009).
18. M. Law *et al.*, *Nano Lett.* **8**, 3904 (2008).
19. D. V. Talapin, C. B. Murray, *Science* **310**, 86 (2005).
20. Y. Liu *et al.*, *Nano Lett.* **10**, 1960 (2010).
21. J. M. Luther *et al.*, *Nano Lett.* **8**, 3488 (2008).
22. K. S. Leschkies, T. J. Beatty, M. S. Kang, D. J. Norris, E. S. Aydil, *ACS Nano* **3**, 3638 (2009).
23. J. J. Choi *et al.*, *Nano Lett.* **9**, 3749 (2009).
24. See the supporting material on *Science* Online for a complete description of materials synthesis; device fabrication, characterization, and modeling; and details of the MEG model used in Fig. 3.
25. J. Gao *et al.*, *Nano Lett.* **11**, 1002 (2011).
26. R. Y. Wang *et al.*, *Nano Lett.* **8**, 2283 (2008).
27. W. Ma *et al.*, *ACS Nano* **5**, 8140 (2011).
28. J. Tang *et al.*, *Nat. Mater.* **10**, 765 (2011).
29. M. Wolf, R. Brendel, J. H. Werner, H. J. Queisser, *J. Appl. Phys.* **83**, 4213 (1998).
30. J. J. H. Pijpers *et al.*, *Nat. Phys.* **5**, 811 (2009).
31. N. M. Gabor, Z. H. Zhong, K. Bosnick, J. Park, P. L. McEuen, *Science* **325**, 1367 (2009).
32. S. J. Wang, M. Khafizov, X. M. Tu, M. Zheng, T. D. Krauss, *Nano Lett.* **10**, 2381 (2010).
33. P. D. Cunningham *et al.*, *Nano Lett.* **11**, 3476 (2011).
34. W. Shockley, H. Queisser, *J. Appl. Phys.* **32**, 510 (1961).

Acknowledgments: We thank M. C. Hanna, K. Emery, B. K. Hughes, K. S. Mistry, and M. R. Bergren for helpful discussions and B. To for SEM imaging. This work was supported by the Center for Advanced Solar Photophysics, an Energy Frontier Research Center funded by the U.S. Department of Energy (DOE), Office of Science, Office of Basic Energy Sciences (BES). DOE funding was provided to the National Renewable Energy Laboratory (NREL) through contract DE-AC36-08GO28308. NREL has filed a patent related to this work.

Supporting Online Material

www.sciencemag.org/cgi/content/full/334/6062/1530/DC1
Materials and Methods
SOM Text
Figs. S1 to S10
Table S1
References (*35*–*39*)

15 July 2011; accepted 11 November 2011
10.1126/science.1209845

Growth of Uniformly Oriented Silica MFI and BEA Zeolite Films on Substrates

Tung Cao Thanh Pham, Hyun Sung Kim, Kyung Byung Yoon*

Applications of zeolite films benefit from alignment of the integrated channels, but methods for film growth have nearly always introduced orientational randomization in the direction normal to the substrate. We now report facile methods to grow silicalite-1 films and pure silica beta zeolite films on substrates with straight or sinusoidal channels positioned uniformly upright at a thickness of up to 8 micrometers. Precise gel compositions and processing temperatures are critical to promote secondary growth on pre-formed oriented crystal monolayers while suppressing self-crystallization in the bulk medium. Preliminary results highlight the potential of these uniformly oriented films in the nonlinear optical response and separation of xylene isomers.

Zeolites are aluminosilicates with angstrom-scale pores and channels in their crystal lattice. When grown as continuous films on various substrates, they function as molecular sieve membranes (*1*–*13*) and platforms for second-order nonlinear optical (2-NLO) mixing (*14*–*16*), among other applications (*17*–*20*). In these contexts, optimal performances would be expected when the channel directions were uniformly oriented normal to the substrate planes from the top to the bottom of the films. However, despite great effort over the past three decades (*1*–*13*, *21*, *22*), uniformity in the channel orientation of zeolite films has not been achieved.

For example, silicalite-1 (SL) is a pure silica MFI (*23*) zeolite with 5.5 × 5.1 Å–sized elliptical channels running along the *a* axis in a sinusoidal manner and 5.6 × 5.3 Å–sized elliptical channels running straight along the *b* axis (Fig. 1, A and B) (*24*). Previous attempts to grow it as a continuous film with the sinusoidal (*a*-axis) and straight (*b*-axis) channels pointing perfectly normal to the substrates have not been successful (*3*, *6*–*10*, *12*). Another zeolite, beta (BEA) (*23*), adopts a truncated bipyramidal shape, with 6.6 × 6.7 Å channels running straight along the *a* (or *b*) axis and

Korea Center for Artificial Photosynthesis and Department of Chemistry, Sogang University, Seoul 121-742, Korea.

*To whom correspondence should be addressed. E-mail: yoonkb@sogang.ac.kr

5.6 × 5.6 Å channels running tortuously along the *c* axis (Fig. 1C) (*25*, *26*). In attempts to grow pure silica BEA (Si-BEA) films on substrates, there have been no reports of films with the *a* (or *b*) axis uniformly normal to the substrate (*27*–*29*).

The typical procedures used in the past for the growth of oriented SL films are as follows [see supporting online material (SOM) text for more details]. In the case of SL films, initially prepared leaflet-shaped (Fig. 1A) and coffin-shaped (Fig. 1B) crystals are assembled into *a*-oriented (*9*) (*a* axis normal to the substrate plane) (Fig. 1D) and *b*-oriented (*30*) (*b* axis normal to the substrate plane) (Fig. 1E) monolayers on appropriate substrates. [In the case of Si-BEA films, *a*-oriented monolayer assembly of Si-BEA crystals (Fig. 1F) has not even been attempted.] The substrates coated with SL monolayers are then immersed in a synthesis gel consisting of water, tetraethylorthosilicate (TEOS), and either tetrapropylammonium hydroxide (TPAOH) or *bis*-*N*,*N*-(tripropylammoniumhexamethylene) di-*N*,*N*-propylammoniumtrihydroxide (*trimer*-TPAOH), which is subsequently heated in a Teflon-lined autoclave (*9*, *31*) at desired temperatures for appropriate periods of time. The use of TPAOH or *trimer*-TPAOH is essential for the syntheses of SL films, because the TPA^+ ion (or TPA^+ analogs in *trimer*-TPAOH) acts as the structure-directing agent. As a result, these ions become entrapped at the intersections between the sinusoidal and straight channels, thereby blocking the channels, and they must be removed from the SL films by calcination (usually by heating at 550°C for 12 hours under flowing oxygen or air) before the films can be used for separation and adsorption.

The crucial problem is that the above procedure always leads to the growth of randomly oriented SL films on seed crystals, regardless of the seed crystals' orientations on substrates or the thickness of the newly grown films. As a result, the sinusoidal channels running along the *a* axis and the straight channels running along the *b* axis become randomly oriented within the films, with large degrees of channel discontinuity at various positions owing to large degrees of local crystal orientation mismatches. The randomly oriented films also have an intrinsically high propensity to crack during the calcination step owing to the complex thermal expansion coefficients of SL grains along each principal axis (*32*, *33*), which vary significantly not only in magnitude but also in sign in the temperature range between room temperature and the calcination temperature (table S1).

Here we report improved membrane preparation methods that reproducibly yield uniformly *a*- (Fig. 1G) and *b*-oriented (Fig. 1H) SL and Si-BEA (Fig. 1I) membranes on substrates. We furthermore demonstrated preliminary application of *b*-oriented SL membranes for the preparation of 2-NLO films and for the separation of a mixture of ortho- and para-xylenes.

We first prepared leaflet-shaped SL crystals (0.3 × 1.3 × 1.5 μm^3) (fig. S1 and SOM methods), rounded coffin-shaped SL crystals with four different sizes (0.35 × 0.12 × 0.7, 1.0 × 0.5 × 1.4, 1.5 × 0.6 × 1.9, and 2.8 × 1.1 × 4.8 μm^3) (fig. S2), and truncated bipyramidal Si-BEA crystals (14 × 14 × 19 μm^3) (fig S3). These were assembled into uniformly oriented monolayers on glass plates by rubbing (*30*, *34*) (Fig. 2, A to C), and secondary growth was conducted on the surfaces (SOM methods). The key to successful growth of uniformly oriented films was to prepare appropriate gel compositions and find appropriate reaction temperatures. After ~1000 trials, we discovered three optimal gels (SOM methods). Gel-1 was composed of fumed silica, tetraethylammonium hydroxide (TEAOH), ammonium hexafluorosilicate [$(NH_4)_2SiF_6$], KOH, and H_2O in a mole ratio of 4.00:1.92:0.36:0.40:n_1, where n_1 = 30 to 80. Gel-2 was composed of TEOS, TEAOH, $(NH_4)_2SiF_6$, and H_2O in a mole ratio of 4.00:1.92:0.36:n_2, where n_2 = 40 to 80. Gel-3 was composed of TEOS, TEAOH, hydrogen fluoride, and H_2O in a mole ratio of 4.00:2.20:2.20:n_3, where n_3 = 30 to 40. Gel-1 was a dry powder, whereas gel-2 and gel-3 were semisolids.

When secondary growth on the glass-supported SL leaflet monolayer (*a*-SL_m/g) was conducted in gel-1 at 150°C, nearly perfectly *a*-oriented continuous films steadily grew with time on the *a*-oriented seed monolayers (despite the fact that

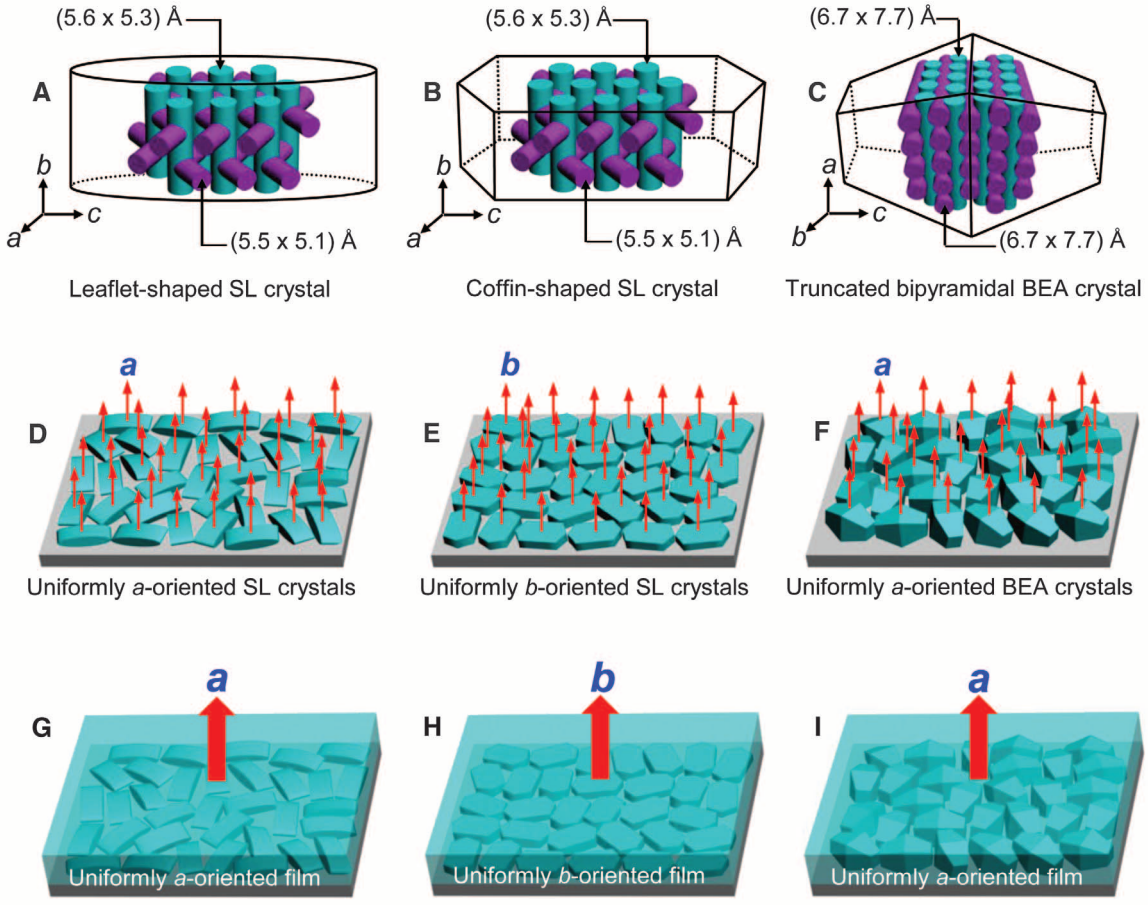

Fig. 1. Schematic illustrations of **(A)** leaflet-shaped and **(B)** coffin-shaped SL crystals and **(C)** truncated bipyramidal BEA crystals and their channel systems, as well as their respective **(D)** *a*-oriented, **(E)** *b*-oriented, and **(F)** *a*-oriented monolayers. **(G** to **I)** Secondary growth on these monolayers produces uniformly oriented films.

gel-1 was a dry powder) (*35*) as demonstrated by the top (Fig. 2D) and side (Fig. 2E) scanning electron microscopy (SEM) views of a film grown over 2 days. The x-ray diffraction pattern of the film (Fig. 2F) shows peaks assigned to diffraction from the (200), (400), (600), (800), and (1000) planes. The weak (501) plane diffraction arises from the slight tilt of the leaflet SL crystals in the monolayers.

When secondary growth on the coffin-shaped SL monolayer (*b*-SL_m/g) was conducted in semisolid gel-2 at 165°C, perfectly *b*-oriented continuous films steadily grew with time on the *b*-oriented seed monolayers, as demonstrated by the top (Fig. 2G) and side (Fig. 2H) SEM views of a film grown over 7 days. The x-ray diffraction pattern of the film (Fig. 2I) only shows the diffraction peaks from the (020), (040), (060), (080), and (0100) planes. The splitting of the latter four diffraction peaks is due to the presence of two different wavelengths in the x-ray source (Cu $K\alpha_1$ and $K\alpha_2$).

When secondary growth on the Si-BEA monolayer (*a*-Si-BEA_m/g) was conducted in semisolid gel-3 at 150°C, nearly perfectly *a*-oriented continuous films steadily grew with time on the *a*-oriented seed monolayers, as demonstrated by the top (Fig. 2J) and side (Fig. 2K) SEM views of a film grown over 4 days. The x-ray diffraction pattern of the film (Fig. 2L) shows the diffraction peaks from the (101) and (116) planes but not from (h00) planes. This pattern is consistent because the Si-BEA crystals are lying on the substrate with one of the four trapezoidal faces parallel to the substrate surface.

For comparison, we also conducted secondary growth on *a*-SL_m/g, *b*-SL_m/g, and *a*-Si-BEA_m/g substrates under the conditions leading to the formation of seed crystals. For this purpose, gels composed of TEOS, TPAOH, and H_2O in a mole ratio of 4:1:600 (TPA gel); of TEOS, *trimer*-TPAOH, KOH, and H_2O in a mole ratio of 4.0:0.5:0.8:950.0 (*t*-TPA gel); and of fumed silica, TEAOH, $(NH_4)_2SiF_6$, KOH, and DDW in a mole ratio of 4.00:1.92:0.36:0.40:31.20 (Si-BEA seed gel) were prepared. The composition of the Si-BEA seed gel was the same as one of the compositions of gel-1. The key differences were that for seed crystal formation, the water content was set more precisely and the temperature was higher (165°C). Otherwise, crystallization did not proceed.

In the case of the secondary growth of *b*-SL_m/g plates in the TPA gel, the *b*-oriented seed crystals (1.0 × 0.5 × 1.4 μm^3) grew bigger even after only 3 hours at 165°C, leading to the formation of continuous films (fig. S4). Simultaneously, *a*-oriented SL crystals also started growing on the *b*-oriented continuous films, and new *b*-oriented SL crystals became attached on the *b*-oriented films. As a result, the surface became very rough. After 24 hours, the film grew much thicker (~10 μm), but the orientations of the SL became highly random as the top (Fig. 3A) and side (Fig. 3B) SEM views show. The x-ray diffraction pattern of the film (Fig. 3C) correspondingly shows peaks arising from other orientations.

Thus, the degree of random orientation increases with time in the TPA gel. Because this phenomenon is unavoidable, attempts have been made to reduce the orientational randomization by conducting a short-period (3 hours) secondary growth in a highly nutrient-depleted TPAOH gel (*21*) or in a gel with very low TPAOH concentration (*22*). However, careful analyses of the films produced by these methods revealed that randomly oriented impure crystals had already begun to form even during the 3-hour period, or the gaps between the crystals were not yet completely filled. After a longer period of time, however, the orientation randomization became more obvious (fig. S5).

In the *t*-TPA gel at 175°C, most of the crystals interconnected very well even after 3 hours, giving rise to the formation of a very smooth continuous film as the top and the cross-sectional SEM views show (fig. S6). During this period, the film thickness increased by 200 nm. Even after 24 hours, the film surface still remained smooth, as the top (Fig. 3D) and side (Fig. 3E) SEM images show, unlike the case of the TPA gel. However, the x-ray diffraction pattern of the SL film (Fig. 3F) showed that both *a* and *b* orientations coexisted. Specifically, the *a*:*b* orientation ratio was 7:3 despite the fact that the seed layer was perfectly *b*-oriented, indicating that leaf-shaped SL crystals produced in the bulk become readily attached to the *b*-oriented seed layer during the secondary growth.

In the case of *a*-SL_m/g plates, the use of TPA gel or *t*-TPA gel instead of gel-1 also led to randomly oriented SL films even after 3 hours at 175°C (figs. S7 and S8). In the case of *a*-Si-BEA_m/g plates, the use of Si-BEA seed gel (the gel used to produce Si-BEA seed crystals) instead of gel-3 led to the formation of randomly oriented films (fig. S9). Even if gel-3 was used for the secondary growth of *a*-Si-BEA_m/g plates, the resulting Si-BEA film became randomly oriented when monolayers of randomly oriented monolayer Si-BEA crystals were used (fig. S10). The use of TPA gel led to the attachment of SL

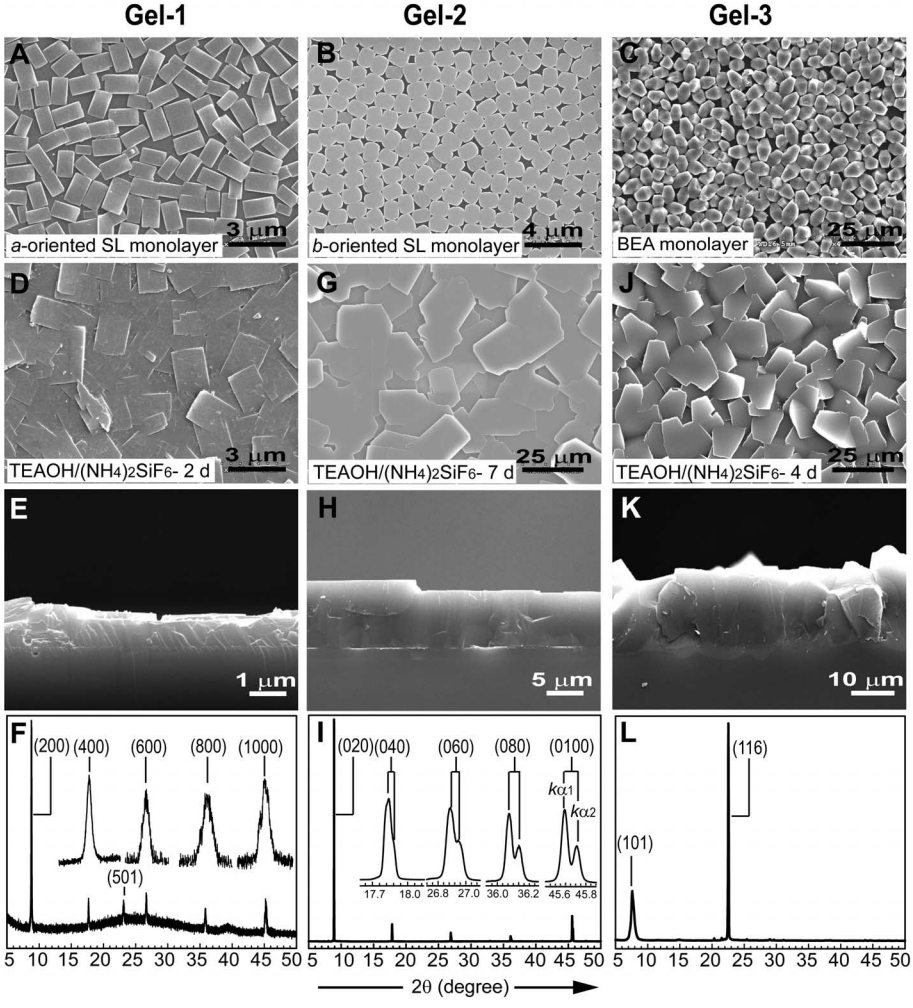

Fig. 2. SEM images of typical (**A**) *a*-oriented and (**B**) *b*-oriented monolayers of SL crystals and (**C**) a monolayer of *a*-oriented Si-BEA crystals assembled on glass plates. Shown below are the respective (**D**, **G**, and **J**) top-view SEM images, (**E**, **H**, and **K**) side-view SEM images, and (**F**, **I**, and **L**) x-ray diffraction patterns of the uniformly oriented continuous films grown on these monolayers under the conditions indicated.

crystals on the surface, and the use of highly basic gel such as the gel for the preparation zeolite Y led to dissolution of the seed Si-BEA crystals (fig. S9).

Another common phenomenon associated with the use of TPA and *t*-TPA gels is that during secondary growth, large amounts of SL crystals form by self-crystallization, independent of the film growth process. Here we define the selectivity of a gel to film formation (S_f in percent) as follows (Eq. 1)

$$S_f\,(\%) = \Delta W_f/(\Delta W_f + W_b) \times 100 \quad (1)$$

where ΔW_f represents the weight of SL film added onto the seed layer, and W_b represents the weight of free SL powder produced in the bulk. In the case of TPA gel, S_f values were 3.11 and 3.23% after 3 and 24 hours, respectively, with ΔW_f and W_b values of 4.4 and 137.2 mg and 14.6 and 436.7 mg, respectively. In the case of *t*-TPA gel, S_f values were 3.16 and 0.34% after 3 and 24 hours, respectively, with ΔW_f and W_b values of 0.5 and 14.4 mg and 0.5 and 307.7 mg, respectively. Thus, in the cases of conventional gels, more than 96% of the nutrients were consumed for the production of SL crystals in the bulk by self-crystallization.

In contrast, gel-1, gel-2, and gel-3 did not form new SL or Si-BEA crystals in the bulk during reaction periods monitored for up to 7 days. In other words, S_f values were 100% in these three gels. As a typical example, the plots of S_f values with respect to reaction time are compared in fig. S11 for the secondary growths of *b*-SL_m/g in gel-2, TPA gel, and *t*-TPA gel.

In the case of secondary growth of *b*-SL_m/g in gel-2, the thickness increased linearly with time for a given thickness of the seed crystal layer and a given reaction temperature (*36*), within experimental error (fig. S12). This first-order kinetic behavior is consistent with the absence of self-crystallization in the gel, a constant SL surface area, the same orientation of the SL surface, and the same reactivity of the SL surface in the same orientation toward the nutrients in the gel. This phenomenon furthermore allows precise control over the desired thickness of the uniformly oriented SL films, by choosing seed crystals with proper thickness (*37*), reaction time, and reaction temperature.

Thus, although the TEA^+ ion alone cannot act as a structure-directing agent to initiate self-nucleation of SL crystals in the gel, it can readily engender secondary growth of SL seed crystals when combined with the F^- source. An independent experiment tracking secondary growth of SL seed crystals dispersed in gel-2 showed that the relative growth rates along the *a*, *b*, and *c* directions were *a*:*b*:*c* = 1:3:15 (fig. S13). Thus, the secondary growth rate along the *c* direction was still much higher than along the other two directions in gel-2 (SOM text).

The above results suggest that self-crystallization in the gel, subsequent diffusion of the self-formed crystals onto the films, and their ensuing attachment in various orientations are the main causes of randomly oriented SL film growth in TPA and *t*-TPA gels. In other words, maintaining secondary growth while inhibiting self-crystallization is the key to achieving orientation control in film growth. The use of tetramethylammonium hydroxide (TMAOH) and tetra-*n*-butylammonium hydroxide (TBAOH) in place of TEAOH in gel-1, gel-2, and gel-3 gives similar results (fig. S14). We also found that the gels remaining after secondary growth could be reused at least three more times by immersing fresh *a*-SL/g, *b*-SL/g, and *a*-Si-BEA/g plates into them.

The randomly oriented polycrystalline SL films (Fig. 3, A and D) readily underwent crack formation upon calcination at 500°C (fig. S15) (increasing the temperature at 100°C $hour^{-1}$), caused by the aforementioned complex temperature-dependent anisotropic thermal expansion coefficients of SL crystals. Recently, Tsapatsis *et al*. demonstrated that a sequence of very rapid (1 min) heating to 700°C, followed by a short (30 s) rest period and very rapid (1 min) cooling to room temperature, leads to stronger binding between the randomly oriented crystals, giving rise to effective suppression of crack formation during calcination (*4*). Uniformly oriented SL and Si-BEA films (Fig. 2, D, G, and J) do not undergo crack formation during or after 24 hours calcination at 550°C, despite the fact that the lattice is still randomly oriented along the other two axes (*a* and *c*). Accordingly, rapid thermal annealing was not necessary to prevent crack formation. In the case of *b*-oriented SL films, this stability against crack formation was confirmed not only by thorough SEM analyses of the surfaces but also by the observation that 1,3,5-triisopropylbenzene does not diffuse through the calcined *b*-oriented films supported on porous silica, as described in more detail below. Laser scanning confocal microscopy also confirmed the absence of crack formation during calcination (fig. S16).

In the initial period after the development of gel compositions, we routinely observed that the uniformly oriented SL films became contaminated with small randomly oriented crystals as the film thickness increased (fig. S17). Later we figured out that the surfaces of the seed crystals

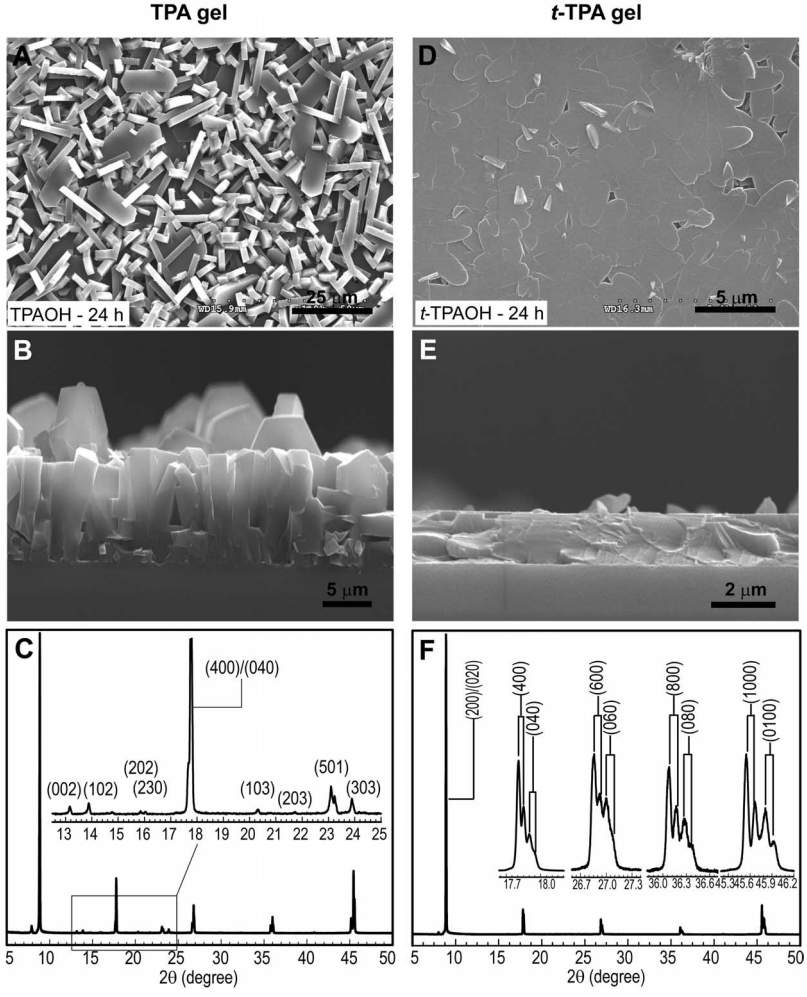

Fig. 3. Respective (**A** and **D**) top-view and (**B** and **E**) side-view SEM images and (**C** and **F**) x-ray diffraction patterns of randomly oriented SL films supported on glass, obtained by secondary growth of *b*-SL_m/g in TPA gel; and randomly oriented SL films supported on glass, obtained by secondary growth of *b*-SL_m/g in *t*-TPA gel.

become covered with an amorphous silica layer with a thickness of ~7 nm (fig. S18) during the processes of monolayer assembly by rubbing and subsequent calcination to affix them onto substrates, and that the outermost amorphous silica layer was responsible for the contamination. The outermost amorphous silica layers were effectively removed by treating the calcined SL seed crystals with a 0.2 M NH_4F solution for 6 hours. The freshly exposed *b*-oriented faces (fig. S18) served as the true template surface for the subsequent growth of the SL films in the *b* orientation, maintaining uniformity up to thicknesses of 8 μm. Without this treatment, the *b*-oriented films became contaminated with small randomly oriented crystals as the thickness increased.

A critical factor for practical application of the SL films is the percentage of straight channels that are open from the top to the bottom of the film. Using the *b*-oriented SL film (Fig. 2D) as an example, we measured this property by counting the number of 1-bromododecane molecules incorporated into the film after saturation (fig. S19 and SOM methods). The *b*-oriented SL films were first washed with a 0.2 M NH_4F solution to remove amorphous layers from the surface and were subsequently dehydrated before immersion in neat 1-bromododecane. After immersion, the air inside the chamber was removed by a brief evacuation at room temperature. After 3, 5, and 7 days of immersion under a reduced pressure, the films were removed from 1-bromododecane and washed with *n*-hexane.

The depth profiles measured by energy-dispersive x-ray spectroscopy showed increasing Br content (atom %) (fig. S20) with increasing immersion time and depth. The gradual decrease of Br content from the bottom to the surface was probably caused by the hexane surface-washing step, because the SL channels have a higher affinity for *n*-hexane than for 1-bromododecane (*10*, *38*). The important point, however, is that 1-bromododecane penetrates to the bottom of the film. This result was further confirmed by our calculation (from the gas chromatographic data) that 1459 molecules of 1-bromododecane were incorporated into a single 3-μm-long SL channel, which corresponds to 87.8% of the theoretical maximum (1662 molecules per channel) (SOM methods).

To explore prospective applications, we first incorporated hemicyanine dyes with varying chain lengths (Fig. 4A) into uniformly *b*-oriented SL films with a range of thicknesses (0.13, 2.40, 2.60, and 3.00 μm) and measured their 2-NLO activities. To compare with previously reported results (*14*), we also incorporated HC-*n* dyes into *b*-oriented SL films grown directly on bare glass plates (primary growth films, with a measured thickness of 400 nm).

The profiles of the number of HC-*n* molecules incorporated into a single SL channel [$(N_C)_n$] with respect to the chain length *n* in HC-*n* are shown in Fig. 4B for each SL film (SOM methods). In the case of uniformly *b*-oriented films, $(N_C)_n$ increased as the thickness of the film was increased. Furthermore, $(N_C)_n$ progressively increased with increasing chain length *n* until *n* = 15 and progressively decreased with further increasing *n*. In the case of the primary growth film, however, $(N_C)_n$ progressively decreased with increasing *n* (*14*). These results show that the uniformly *b*-oriented SL films are more hydrophobic than the primary growth film. The $(N_C)_n$ value of 16 observed for the 130-nm-thick SL film for the case of HC-15 is a very large increase when compared with the value of ~6 observed for the 400-nm-thick primary growth film (*14*). The measured $(N_C)_n$ values for the SL film prepared using the *t*-TPA gel were always smaller than those measured for the 130-nm-thick uniformly *b*-oriented SL film, despite the fact that the thickness of the former is 10 times thicker (1.3 μm).

The relative second harmonic intensities (rel-$I_{2\omega}$) induced by irradiation of SL films (*p*-polarized $I_{2\omega}$ generated from a *p*-polarized 1064-nm fundamental laser beam) with respect to that of a 3-mm-thick, Y-cut quartz plate were obtained by the Maker fringe method (fig. S21), and they are plotted with respect to *n* for each thickness (Fig. 4C). The plot shows that even 2.4- to 3.0-μm-thick HC-*n*–incorporating SL films (*n* = 12, 15, 18, and 22) have higher second-order NLO activities than a thousand times thicker (3 mm) quartz, which is often used as the reference material (*14*). The highest rel-$I_{2\omega}$ value (174.5%) was obtained from the HC-15–incorporating 3.0-μm-thick SL film (table S2). This value also corresponds to a 21-fold increase with respect to the highest value previously observed using HC-*n*–incorporating primary growth SL films (8%) (*14*). The measured rel-$I_{2\omega}$ values observed for the SL film prepared by *t*-TPA gel were always smaller than 7.1%.

The calculated d_{33} values (a tensor component of the quadratic nonlinear susceptibility of a 2-NLO material) for HC-*n*–incorporating SL films are tabulated in table S2. In the case of HC-15, the d_{33} values are between 2.68 (3-μm film) and 35.42 pm/V (0.13-μm film). Corresponding values of commercial 2-NLO materials range from 0.16 to 13.7 pm/V (table S3). Thus, uniformly *b*-oriented HC-15–incorporating SL films have potential for development into commercially viable 2-NLO materials. In contrast, the d_{33} value of the SL film prepared from *t*-TPA gel was 1.21 pm/V, indicating that it is less suitable for commercial applications (table S4).

Furthermore, the 2-μm-thick uniformly *b*-oriented films showed transparencies (70 to 84% in the 380- to 1100-nm region) comparable to those of plain glass (~85%) (figs. S22 and S23). The corresponding values observed from the

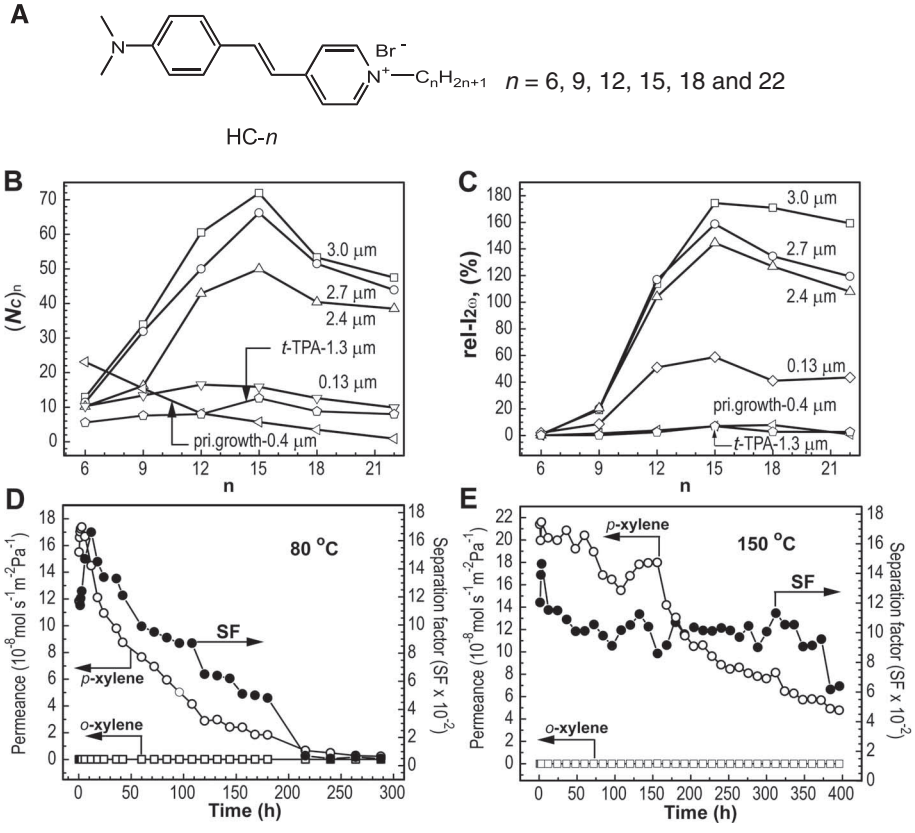

Fig. 4. (**A**) Structure of HC-*n* dyes. (**B**) Plots of the number of HC-*n* dyes incorporated in a single channel $(N_C)_n$ of the SL film versus the alkyl chain length *n* of the HC-*n* dye. (**C**) Plots of the relative second harmonic intensity (rel-$I_{2\omega}$) of the HC-*n*–incorporating SL films (of indicated thickness) with respect to a reference (3-mm-thick Y-cut quartz) versus the alkyl chain length *n* of the HC-*n* dye. Below are plots of permeances of *p*- (open circle) and *o*-xylene (open square) and the SF with time for the two operation temperatures, (**D**) 80°C and (**E**) 150°C.

random SL films were 20 to 60% when prepared from the *t*-TPA gel and below 12% when prepared from the TPA gel.

Another major application of zeolite films is in membrane-mediated separation of small-molecule mixtures into pure components. The separation of xylenes has received particular attention (*4*, *8*). To investigate the performance of uniformly *b*-oriented SL films as xylene mixture-separation membranes, we prepared monolayers of rounded coffin-shaped SL crystals on porous silica supports and subsequently grew 1.0-μm-thick uniformly *b*-oriented SL films (fig. S24) in gel-2 (SOM methods). The use of porous silica supports is necessary to maintain uniform *b*-orientation of the SL films, because aluminum-containing porous supports suppress the film growth. The preparation of the porous silica supports was readily achieved by one step: 2 hours of calcination at 1020°C (SOM methods). The separation of the *o*- and *p*-xylene mixture was conducted at two different temperatures (80° and 150°C) under standard reported conditions (SOM methods and fig. S25).

The initially measured permeance of *p*-xylene at 80°C was much higher than that of *o*-xylene, giving rise to a high (>1900) separation factor (SF) (Fig. 4D). However, the permeances continuously decreased over a period of 216 hours and reached a steady state. The steady-state permeances of *p*-xylene and *o*-xylene were 0.7×10^{-8} and 0.0092×10^{-8} mol s^{-1} m^{-2} Pa^{-1}, respectively, giving rise to a steady-state SF of 71. We attribute the continuous decreases of *p*-xylene permeance and the SF value to gradual adsorption of *o*-xylene into the channels, leading to a gradual increase in the degree of channel blockage, which in turn decreases the diffusion rate of *p*-xylene molecules (*11*). The fact that the permeance decreases to near zero also indicates that the *b*-oriented SL film does not have cracks.

At 150°C, the *p*-xylene permeance also continuously decreased from 21.6×10^{-8} to 5×10^{-8} mol s^{-1} m^{-2} Pa^{-1} over a period of 400 hours (Fig. 4E). During the same period, the *o*-xylene permeance decreased from 0.0097×10^{-8} to 0.0068×10^{-8} mol s^{-1} m^{-2} Pa^{-1}. The gradual decrease of *p*-xylene permeance even at 150°C indicates that the channel blocking by *o*-xylene still continues at 150°C, and the *b*-oriented SL film does not undergo crack formation during the operation. During the period from 20 to 370 hours, the SF value remained nearly constant at ~1000. Although this steady-state SF value is lower than the highest value observed from randomly oriented tubular SL films (*12*), it is about two times higher than those of randomly oriented non-tubular SL films with similar thickness (table S5).

We have reported straightforward methods to prepare uniformly *a*- and *b*-oriented SL films and *a*-oriented Si-BEA films. The control of orientation is not limited to the channel upright directions but can be applied to any desired directions by finding proper methods to uniformly orient SL and Si-BEA crystals in those directions on supports. We believe our findings will trigger extensions of the methods to the preparation of various other types of zeolite films in perfectly uniform orientations.

References and Notes

1. J. O'Brien-Abraham, J. Y. S. Lin, in *Zeolites in Industrial Separation and Catalysis*, S. Kulprathipanja, Ed. (Wiley VCH, Verlag, Weinheim, Germany, 2010), chap. 3, pp. 307–329.
2. J. Caro, M. Noack, in *Advances in Nanoporous Materials*, S. Ernst, Ed. (Elsevier, Amsterdam, 2009), vol. 1, chap. 1, pp. 1–96.
3. J. Caro, M. Noack, *Microporous Mesoporous Mater.* **115**, 215 (2008).
4. J. Choi *et al.*, *Science* **325**, 590 (2009).
5. J. Hedlund, F. Jareman, A. J. Bons, M. Anthonis, *J. Membr. Sci.* **222**, 163 (2003).
6. Z. P. Lai, M. Tsapatsis, J. R. Nicolich, *Adv. Funct. Mater.* **14**, 716 (2004).
7. C. J. Gump, V. A. Tuan, R. D. Noble, J. L. Falconer, *Ind. Eng. Chem. Res.* **40**, 565 (2001).
8. Z. P. Lai *et al.*, *Science* **300**, 456 (2003).
9. M. A. Snyder, M. Tsapatsis, *Angew. Chem. Int. Ed.* **46**, 7560 (2007).
10. H. H. Funke, A. M. Argo, J. L. Falconer, R. D. Noble, *Ind. Eng. Chem. Res.* **36**, 137 (1997).
11. J. O'Brien-Abraham, M. Kanezashi, Y. S. Lin, *J. Membr. Sci.* **320**, 505 (2008).
12. M. O. Daramola *et al.*, *Sep. Sci. Technol.* **45**, 21 (2009).
13. H. Guo *et al.*, *Angew. Chem. Int. Ed.* **45**, 7053 (2006).
14. H. S. Kim *et al.*, *J. Am. Chem. Soc.* **126**, 673 (2004).
15. H. S. Kim *et al.*, *Adv. Mater.* **19**, 260 (2007).
16. H. S. Kim, T. T. Pham, K. B. Yoon, *J. Am. Chem. Soc.* **130**, 2131 (2008).
17. C. M. Lew, R. Cai, Y. Yan, *Acc. Chem. Res.* **43**, 210 (2010).
18. Z. Li *et al.*, *Angew. Chem. Int. Ed.* **45**, 6329 (2006).
19. M. E. Davis, *Nature* **417**, 813 (2002).
20. T. Bein, *Chem. Mater.* **8**, 1636 (1996).
21. Y. Liu, Y. S. Li, W. S. Yang, *J. Am. Chem. Soc.* **132**, 1768 (2010).
22. X. Li, Y. Peng, Z. Wang, Y. Yan, *CrystEngComm* **13**, 3657 (2011).
23. MFI and BEA are two different framework-type codes assigned by the Structural Commission of the International Zeolite Association. Silicalite-1 and ZSM-5 belong to MFI. ZSM-5 has aluminosilicate frameworks with varying Si/Al ratios, whereas silicalite-1 has a pure silica framework. BEA is also often called beta zeolite. BEA has aluminosilicate frameworks with varying Si/Al ratios, whereas pure silica BEA (Si-BEA) has a pure silica framework.
24. C. Baerlocher, W. M. Meier, D. H. Olson, *Atlas of Zeolite Framework Types* (Elsevier, Amsterdam, ed. 5, 2001), pp. 184–185.
25. O. Larlus, V. Valtchev, *Microporous Mesoporous Mater.* **93**, 55 (2006).
26. O. Larlus, V. Valtchev, *Chem. Mater.* **17**, 881 (2005).
27. A. Mitra *et al.*, *Ind. Eng. Chem. Res.* **43**, 2946 (2004).
28. A. Mitra *et al.*, *J. Electrochem. Soc.* **149**, B472 (2002).
29. S. Mintova, M. Reinelt, T. H. Metzger, J. Senker, T. Bein, *Chem. Commun.* **2003**, 326 (2003).
30. K. B. Yoon, *Acc. Chem. Res.* **40**, 29 (2007).
31. R. Singh, P. K. Dutta, in *Handbook of Zeolite Science and Technology*, S. Auerbach, K. Carrado, P. Dutta, Eds. (Marcel Dekker, New York, 2003), chap. 2.
32. A. Marinkovic *et al.*, *Microporous Mesoporous Mater.* **71**, 117 (2004).
33. D. Bhange, V. Ramaswamy, *Mater. Res. Bull.* **41**, 1392 (2006).
34. J. S. Lee, J. H. Kim, Y. J. Lee, N. C. Jeong, K. B. Yoon, *Angew. Chem. Int. Ed.* **46**, 3087 (2007).
35. The transfer of nutrients from the dry gel to the seed layer seems to be carried out by a small amount of moisture, which vaporizes into steam at the reaction temperature.
36. As the reaction temperature increases, the growth rate increases. However, as a possible means to incorporate more second-order NLO dyes into the channels, we chose the relatively low reaction temperatures (140° to 180°C) with the hypothesis that the number of defect sites in the channels would decrease as the growth rate decreased.
37. The thickness of the seed crystal does not affect the growth rate. However, if one wants to reach the desired thickness faster, it will be beneficial to start with thicker seed crystals.
38. H. Karsli, A. Çulfaz, H. Yücel, *Zeolites* **12**, 728 (1992).

Acknowledgments: This work was supported by the Korea Center for Artificial Photosynthesis, located at Sogang University and funded by the Ministry of Education of Science and Technology through the National Research Foundation of Korea (NRFK) (grant NRF-2009-C1AAA001-2009-0093879) and the acceleration program of the NRFK. We thank J. Y. Lee for help in drawing Fig. 1. Sogang University has filed patents on the results presented here.

Supporting Online Material

www.sciencemag.org/cgi/content/full/334/6062/1533/DC1
Materials and Methods
SOM Text
Figs. S1 to S25
Tables S1 to S5
References (*39*–*42*)

10 August 2011; accepted 8 November 2011
10.1126/science.1212472

Revealing Atom-Radical Reactivity at Low Temperature Through the N + OH Reaction

Julien Daranlot,[1] Mohamed Jorfi,[2] Changjian Xie,[3] Astrid Bergeat,[1] Michel Costes,[1] Philippe Caubet,[1] Daiqian Xie,[3] Hua Guo,[4] Pascal Honvault,[5,6] Kevin M. Hickson[1]*

More than 100 reactions between stable molecules and free radicals have been shown to remain rapid at low temperatures. In contrast, reactions between two unstable radicals have received much less attention due to the added complexity of producing and measuring excess radical concentrations. We performed kinetic experiments on the barrierless $N(^4S) + OH(^2\Pi) \rightarrow H(^2S) + NO(^2\Pi)$ reaction in a supersonic flow (Laval nozzle) reactor. We used a microwave-discharge method to generate atomic nitrogen and a relative-rate method to follow the reaction kinetics. The measured rates agreed well with the results of exact and approximate quantum mechanical calculations. These results also provide insight into the gas-phase formation mechanisms of molecular nitrogen in interstellar clouds.

The chemistry of low-temperature environments, such as interstellar clouds (ISCs), was thought to be governed by reactions involving electrically charged species (*1*) until recent advances in experimental and theoretical methods showed that reactions between uncharged species could occur and even dominate in some low-temperatures regions. The 1990s